LETTER

doi:10.1038/nature25135

Enhancement and sign change of magnetic correlations in a driven quantum many-body system

Frederik Görg[1], Michael Messer[1], Kilian Sandholzer[1], Gregor Jotzu[1,2], Rémi Desbuquois[1] & Tilman Esslinger[1]

Periodic driving can be used to control the properties of a many-body state coherently and to realize phases that are not accessible in static systems. For example, exposing materials to intense laser pulses makes it possible to induce metal–insulator transitions, to control magnetic order and to generate transient superconducting behaviour well above the static transition temperature[1–6]. However, pinning down the mechanisms underlying these phenomena is often difficult because the response of a material to irradiation is governed by complex, many-body dynamics. For static systems, extensive calculations have been performed to explain phenomena such as high-temperature superconductivity[7]. Theoretical analyses of driven many-body Hamiltonians are more challenging, but approaches have now been developed, motivated by recent observations[8–10]. Here we report an experimental quantum simulation in a periodically modulated hexagonal lattice and show that antiferromagnetic correlations in a fermionic many-body system can be reduced, enhanced or even switched to ferromagnetic correlations (sign reversal). We demonstrate that the description of the many-body system using an effective Floquet–Hamiltonian with a renormalized tunnelling energy remains valid in the high-frequency regime by comparing the results to measurements in an equivalent static lattice. For near-resonant driving, the enhancement and sign reversal of correlations is explained by a microscopic model of the system in which the particle tunnelling and magnetic exchange energies can be controlled independently. In combination with the observed sufficiently long lifetimes of the correlations in this system, periodic driving thus provides an alternative way of investigating unconventional pairing in strongly correlated systems experimentally[7,9,10].

The increasing demand for high-speed control of magnetic memory devices in the terahertz frequency regime has led to efforts to control the magnetic properties of materials optically, such as switching from antiferromagnetic to ferromagnetic ordering[4,5]. To engineer suitable materials for future applications, it is desirable to gain a better understanding of the underlying microscopic processes. In this context, experiments using cold atoms provide an ideal platform for investigating driven many-body systems, owing to the slow timescales and the prospect of quantitative comparisons to theoretical predictions. So far, periodic modulation has been used in such set-ups to engineer effective Hamiltonians[11,12], which has enabled Hubbard parameters to be renormalized and classical magnetism to be studied in the high-frequency regime, as well as new features such as topological or spin-dependent band structures to be realized[13–15]. By driving interacting systems[16,17], charge and spin degrees of freedom can both be influenced by addressing density-dependent processes individually[18–20]. Until now, the measurement of magnetic correlations in driven optical lattices has remained an open challenge. An experimental difficulty lies in the heating associated with the periodic modulation of a many-body system, which can destroy correlations, especially in the near-resonant regime[14,21,22].

We perform our experiments using a degenerate Fermi gas consisting of $3.0(2) \times 10^4$ (10% systematic error) ultracold ^{40}K atoms prepared in a balanced mixture of two internal states, denoted as ↑ and ↓ (see Methods). The atoms are loaded into an optical superlattice with a tunable geometry and anisotropic tunnelling rates, whereby the horizontal links in the x direction (t_x) are stronger than those in the y and z directions ($t_{y,z}$; Fig. 1c). In the x–z plane, the lattice consists of hexagonal layers, which are stacked in the y direction. We modulate the lattice position in the x direction periodically in time with a displacement amplitude A at a frequency of $\omega/(2\pi)$, which is achieved by moving the retroreflecting mirror of the optical lattice using a piezoelectric actuator (Fig. 1a).

Our system is well described by the driven Fermi–Hubbard model:

$$\hat{H}(\tau) = -\sum_{\langle i,j\rangle,\sigma} t_{ij}\hat{c}^{\dagger}_{i\sigma}\hat{c}_{j\sigma} + U\sum_{i}\hat{n}_{i\uparrow}\hat{n}_{i\downarrow} + \sum_{i,\sigma}\left[f_i(\tau) + V_i\right]\hat{n}_{i\sigma} \qquad (1)$$

where $\hat{c}^{\dagger}_{i\sigma}$, $\hat{c}_{i\sigma}$ and $\hat{n}_{i\sigma}$ are the fermionic creation, annihilation and number operators, respectively, at site $\boldsymbol{i} = (i_x, i_y, i_z)$ in spin state $\sigma \in \{\uparrow, \downarrow\}$.

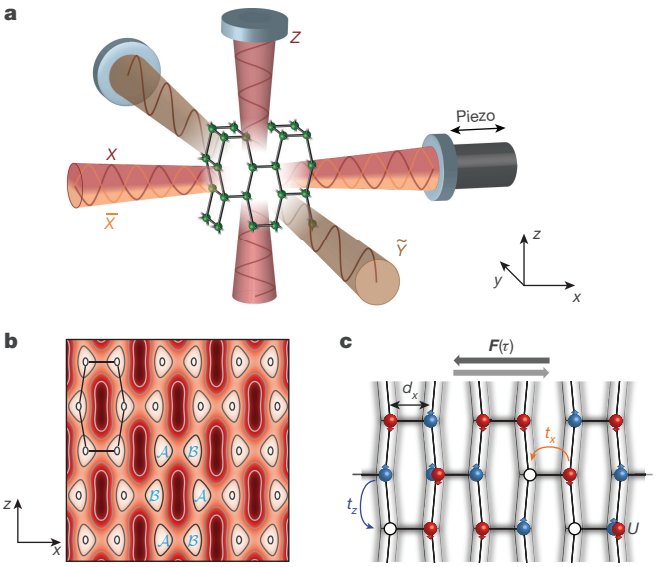

Figure 1 | Experimental set-up. a, Optical set-up used to create the three-dimensional lattice geometry. The beams X and Z are interfering, whereas $\bar{X}$ and $\tilde{Y}$ are frequency-detuned. A piezoelectric actuator sinusoidally modulates the position of the retroreflecting mirror in the x direction. **b**, Lattice potential (colour scale, lighter red corresponds to a lower potential depth) in the x–z plane. The lattice consists of $\mathcal{A}$ and $\mathcal{B}$ sublattices, and a hexagonal unit cell is superimposed. **c**, Tight-binding representation of the lattice potential in the x–z plane. The system is described by a driven Fermi–Hubbard model, with anisotropic tunnelling energies $t_x > t_z$, owing to the shorter length d_x of the horizontal bonds. Atoms in different spin states (red and blue, arrows) interact via an on-site interaction U. In a co-moving frame, the modulation of the lattice position (indicated by grey lattices in the background) corresponds to a linear force $\boldsymbol{F}(\tau)$ in the x direction with an amplitude of $\hbar\omega K_0/d_x$, which primarily influences the horizontal bonds ($\boldsymbol{F}(\tau) = (\hbar\omega K_0/d_x)\cos(\omega\tau)\boldsymbol{e}_x$; Methods).

[1]Institute for Quantum Electronics, ETH Zurich, 8093 Zurich, Switzerland. [2]Max Planck Institute for the Structure and Dynamics of Matter, 22761 Hamburg, Germany.

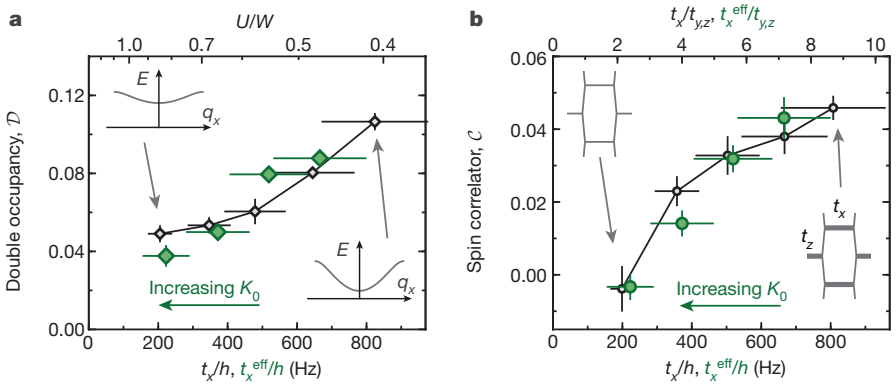

Figure 2 | Description of the driven system by an effective Hamiltonian in the high-frequency regime. a, Double occupancy $\mathcal{D}$ as a function of the effective horizontal tunnelling energy $t_x^{\mathrm{eff}}(K_0) = t_x\mathcal{J}_0(K_0)$ for a driven system (green), and results obtained from an experimental quantum simulation in a static configuration with horizontal tunnelling t_x (black). The insets show cuts through the non-interacting band structure (E, energy) as a function of the quasi-momentum in the x direction q_x. The reduction in the bandwidth W leads to a lower double occupancy, indicating the crossover to a Mott-insulating state. **b**, Spin–spin correlations $\mathcal{C}$ as a function of the (effective) horizontal tunnelling energy for the driven case (green) and an equivalent static configuration (black). The renormalization of the tunnelling energy leads to a reduction in lattice anisotropy $t_x^{\mathrm{eff}}/t_{y,z}$ (see insets), which reduces the magnetic correlations on the horizontal link. The transverse tunnelling energies are $t_y/h = 125(8)$ Hz and $t_z/h = 78(8)$ Hz and the interaction is set to $U/h = 0.93(2)$ kHz. Horizontal error bars reflect the uncertainty in the lattice depth; data points and vertical error bars in **a** (**b**) denote the mean and standard error of 4 (10) individual measurements at different times within one driving period (see Methods).

Here, t_{ij} denotes the tunnelling rate between nearest neighbours $\langle \boldsymbol{i}, \boldsymbol{j}\rangle$, U the repulsive on-site interaction and $V_{\boldsymbol{i}}$ an overall harmonic trapping potential. The time-dependent force is expressed as $f_{\boldsymbol{i}}(\tau) = mA\omega^2 x_{\boldsymbol{i}}\cos(\omega\tau)$, where m is the mass of the atoms and $x_{\boldsymbol{i}} = \langle\hat{x}\rangle_{\boldsymbol{i}}$ is the x position of the Wannier function on site $\boldsymbol{i}$. Therefore, the driving is used primarily to address the bonds in the x direction (Methods). To characterize the many-body state in the lattice, we measure the fraction of atoms on doubly occupied sites

$$\mathcal{D} = \frac{2}{N}\sum_{\boldsymbol{i}\in\mathcal{A},\mathcal{B}} \langle \hat{n}_{\boldsymbol{i}\uparrow}\hat{n}_{\boldsymbol{i}\downarrow}\rangle$$

and the nearest-neighbour spin–spin correlator

$$\mathcal{C} = -\frac{1}{N}\sum_{\boldsymbol{i}\in\mathcal{A}} (\langle \hat{S}^x_{\boldsymbol{i}}\hat{S}^x_{\boldsymbol{i}+\boldsymbol{e}_x}\rangle + \langle \hat{S}^y_{\boldsymbol{i}}\hat{S}^y_{\boldsymbol{i}+\boldsymbol{e}_x}\rangle)$$

on the horizontal links along the x direction. (Here N is the total number of atoms, $\boldsymbol{e}_x$ is the unit vector in the x direction, which connects the sites of the $\mathcal{A}$ and $\mathcal{B}$ sublattices, and $\hat{S}_{\boldsymbol{i}}$ represents the standard spin vector operator on site $\boldsymbol{i}$.) The observables are averaged spatially over the inhomogeneous density distribution in the harmonic trap, which has a geometric mean trapping frequency of $\overline{\omega}_{\mathrm{trap}}/(2\pi) = 84(2)$ Hz, and over one oscillation cycle of the periodic modulation, as indicated by $\langle\ldots\rangle$ (see Methods).

In a first experiment, we investigate the regime in which the driving frequency is much higher than all microscopic energy scales of the system, that is, the tunnelling t and interaction energy U ($\hbar\omega \gg t, U$). In the non-interacting case, the modulation renormalizes the horizontal tunnelling rate by a zeroth-order Bessel function ($\mathcal{J}_0$) and the system can be described by an effective tunnelling energy

$$t_x^{\mathrm{eff}}(K_0) = t_x\mathcal{J}_0(K_0) \qquad (2)$$

where $K_0 = mA\omega d_x/\hbar$ is the normalized driving amplitude, with d_x the length of the horizontal bonds (Fig. 1c)[15]. However, it is not clear *a priori* whether this simple description remains accurate in the many-body context[12]. To verify this, we compare our measurements in the driven system to results obtained using an experimental quantum simulation in a static lattice with a variable tunnelling rate t_x. The reliability of our experiment as a quantum simulator for the magnetic properties of the Hubbard model has previously been benchmarked through quantitative comparisons with state-of-the-art numerical calculations[23,24]. To enter the driven regime in the experiment, we ramp up the lattice modulation amplitude linearly to a final value K_0 within 2 ms, at a frequency of $\omega/(2\pi) = 6$ kHz. Afterwards, we allow for an additional equilibration time of 5 ms before the measurement, during which we maintain a fixed modulation amplitude.

The resulting double occupancies and spin correlations agree well for the driven and static cases, as shown in Fig. 2. This supports the validity of the description of the many-body system by an effective Hamiltonian with a tunnelling rate $t_x^{\mathrm{eff}}(K_0)$. For lower tunnelling energies, the double occupancy decreases as a result of the reduction in the bandwidth W. Therefore, for increasing driving amplitude, the system enters the Mott regime[16]. The modulation not only changes the bandwidth, but also the anisotropy of the lattice, because the ratio $t_x^{\mathrm{eff}}(K_0)/t_{y,z}$ decreases for increasing driving amplitude. This effect manifests in the spin correlator on the horizontal link, which decreases for a weaker anisotropy of the underlying lattice, as observed in previous measurements[25]. When driving for longer times, we find that the lifetime of correlations is reduced to 14(5) ms at $K_0 = 1.26(4)$, compared to 92(16) ms in the static case. Nevertheless, this allows us to observe comparable levels of correlations in the driven and static cases on experimental timescales.

Whereas an off-resonant modulation scheme typically leads to a renormalization of pre-existing parameters, physics that is not accessible in static systems arises for a near-resonant drive. For example, extended terms such as density-dependent tunnelling energies can be engineered, which are not present in the single-band Hubbard model[18–20]. To investigate this regime, we set a large on-site interaction close to the driving frequency ($U \approx l\hbar\omega$, $l \in \mathbb{Z}$) and ramp up the modulation at a frequency of either 3 kHz or 6 kHz within 3.3 ms or 2 ms, respectively. We observe that the effective states in the driven Hamiltonian contain a higher fraction of double occupancies if $U \approx l\hbar\omega$ (Fig. 3a).

Strikingly, we find that the magnetic correlations on the horizontal links depend on both the sign and magnitude of the modulation detuning $\delta = \hbar\omega - U$ (Fig. 3b). For a red-detuned drive ($\delta < 0$), correlations are increased compared to the static case if $|\delta|$ is of the order of a few tunnelling energies t_x. By contrast, when choosing $\delta > 0$, the sign of the spin–spin correlator inverts; that is, the system exhibits ferromagnetic correlations on neighbouring sites in the x direction. If we set a fixed interaction strength and vary the amplitude of the modulation, then we find that correlations increase for $\delta < 0$ and $K_0 \approx 1.3$, before they eventually decrease again (Fig. 3c). For $\delta > 0$, a critical value of the driving strength is required for the system to develop ferromagnetic

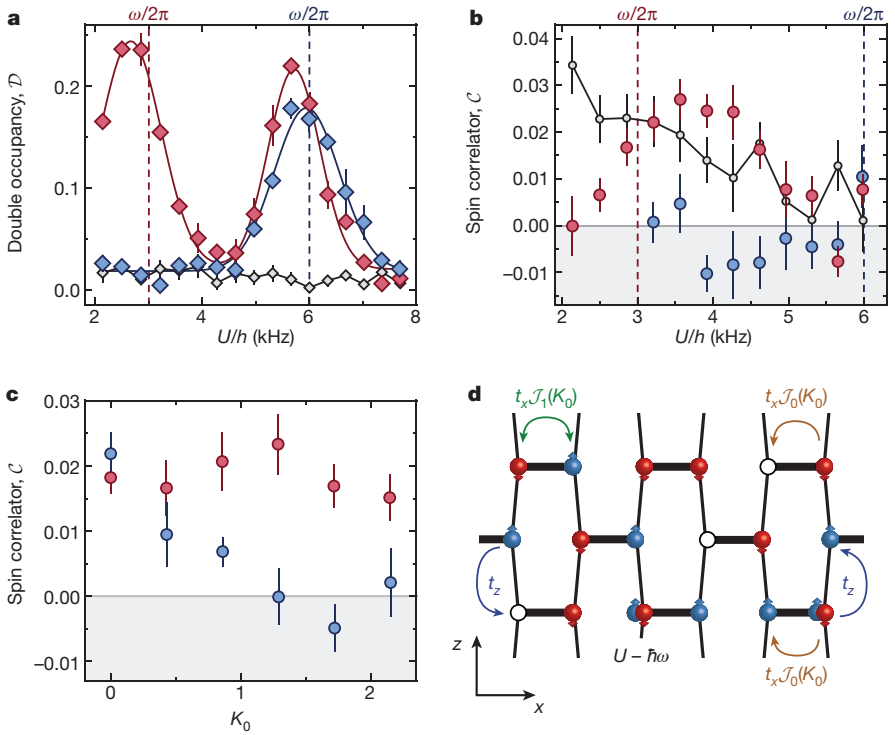

Figure 3 | Enhancement and sign reversal of magnetic correlations by near-resonant driving. a, Double occupancy as a function of on-site interaction U for the static case (black) and for driving frequencies of $\omega/(2\pi) = 3$ kHz (red) or 6 kHz (blue) with a modulation amplitude of $K_0 = 1.30(3)$. Around the resonances (vertical dashed lines), the effective states in the driven Hamiltonian contain a higher number of double occupancies. Solid lines are (double) Gaussian fits to the data. **b**, Spin–spin correlations on the horizontal link as a function of U for the same parameters as in **a**. For $U > \hbar\omega$ (red), antiferromagnetic correlations are enhanced compared to the static case (black) for a broad range of interactions. When $U < \hbar\omega$ (blue), the correlator changes sign and the system develops ferromagnetic correlations. **c**, Spin–spin correlations as a function of driving amplitude K_0 for $\omega/(2\pi) = 3$ kHz and $U/h = 3.8(1)$ kHz (red) or $\omega/(2\pi) = 6$ kHz and $U/h = 4.4(1)$ kHz (blue). For $U > \hbar\omega$, antiferromagnetic correlations increase around $K_0 \approx 1.3$. For $\hbar\omega > U$, correlations become ferromagnetic beyond a critical modulation amplitude. The tunnelling rates are set to $(t_x, t_y, t_z)/h = (570(110), 125(8), 85(8))$ Hz. Data points and error bars in **a** (**b** and **c**) denote the mean and standard error of 4 (10) individual measurements at different times within one driving period (see Methods). **d**, In the near-resonant case ($U \approx \hbar\omega$), the driven system can be described by an effective Hamiltonian in which tunnelling processes that do not change the number of double occupancies are renormalized by $\mathcal{J}_0(K_0)$ (brown). By contrast, the creation of doublon–holon pairs is resonantly enhanced and is determined by the first-order Bessel function $\mathcal{J}_1(K_0)$ (green). The effective interaction of the system becomes $U - \hbar\omega$.

correlations. We also study the time dependence of the magnetic properties, by varying the modulation time after the ramp up of the drive. We find that it takes a few milliseconds for correlations to increase or change sign, but that they ultimately approach zero when driving for long times as a result to heating of the cloud (Extended Data Fig. 1). The lifetime of magnetic correlations as extracted from an exponential fit to the long-time behaviour changes from 82(34) ms in the static case to 12(4) ms at $K_0 = 1.30(3)$. In addition, we observe the fast dynamics within one period of the drive (the so-called micromotion) in our measurement regime (Extended Data Fig. 2). Finally, we investigate the adiabaticity of the preparation protocol by reverting the driving ramp and find that correlations return only partially to their static values (Extended Data Fig. 3).

To obtain an understanding of the observed phenomena at the microscopic scale, we perform a Floquet analysis on the time-periodic Hamiltonian in equation (1) in the near-resonant driving regime with $t \ll U \approx l\hbar\omega$. For that, we switch to a rotating frame with respect to the operator

$$\hat{R}(\tau) = \exp\left\{ i\sum_j \left[l\omega\tau \hat{n}_{j\uparrow}\hat{n}_{j\downarrow} + \sum_\sigma F_j(\tau)\hat{n}_{j\sigma} \right] \right\}$$

where

$$F_j(\tau) = \frac{1}{\hbar}\int_0^\tau f_j(\tau')\mathrm{d}\tau'$$

In this frame, the tunnelling on the horizontal bonds is to lowest order in $1/\omega$ described by the effective Hamiltonian

$$\hat{H}^{\mathrm{eff}}_{t_x} = -t_x \sum_{\substack{i\in\mathcal{A},\sigma \\ j=i+e_x}} \left[\mathcal{J}_0(K_0)\hat{a}_{ij\bar{\sigma}} + \mathcal{J}_l(K_0)\hat{b}^l_{ij\bar{\sigma}} \right] \hat{c}^\dagger_{i\sigma}\hat{c}_{j\sigma} + \mathrm{h.c.} \qquad (3)$$

where $\bar{\uparrow} = \downarrow$ and vice versa[26–28]. Here, the effective tunnelling energy is density-dependent: hopping processes that do not change the number of double occupancies as described by the operator $\hat{a}_{ij\sigma} = (1-\hat{n}_{i\sigma})(1-\hat{n}_{j\sigma}) + \hat{n}_{i\sigma}\hat{n}_{j\sigma}$ are renormalized by $\mathcal{J}_0(K_0)$. In contrast, the creation or annihilation of doublon–holon pairs corresponding to $\hat{b}^l_{ij\sigma} = (-1)^l(1-\hat{n}_{i\sigma})\hat{n}_{j\sigma} + \hat{n}_{i\sigma}(1-\hat{n}_{j\sigma})$ become resonantly restored with an amplitude $t_x\mathcal{J}_l(K_0)$ (Fig. 3d). In addition, the effective interaction $U^{\mathrm{eff}} = U - l\hbar\omega = -\delta_l$ is given by the detuning from the l-photon resonance δ_l. In this picture, we can understand the creation of double occupancies for small δ_l shown in Fig. 3a as the system becoming effectively more weakly interacting.

The magnetic properties of the many-body state are altered substantially in the effective Hamiltonian in equation (3) because at the microscopic scale the superexchange process that leads to spin–spin interactions involves two virtual hopping processes determined by $\mathcal{J}_l(K_0)$, in which a double occupancy at energy U^{eff} is created and annihilated. Therefore, the exchange energy J_{ex}, which is the energy splitting between a spin singlet and triplet state on the horizontal bonds, will depend on both the modulation amplitude K_0 and the detuning δ. It can even change sign for $\delta > 0$, because in this case the effective

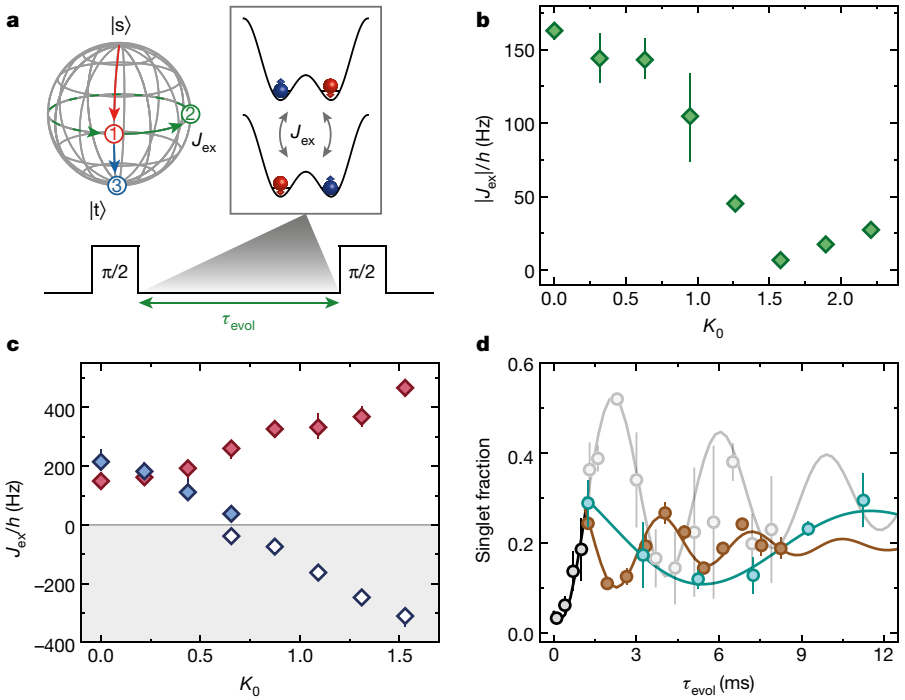

Figure 4 | Magnetic exchange energy for off- and near-resonant driving. **a**, The exchange J_{ex} is measured by preparing local singlet states $|s\rangle$ on isolated double wells. In a Ramsey-type sequence, a superposition between the singlet $|s\rangle$ and triplet $|t\rangle$ states is first created by performing a $\pi/2$ pulse (red arrow) with a magnetic field gradient. The exchange oscillation (green arrow; the solid component represents the one-quarter-oscillation evolution time used in **d**) is then triggered by suddenly lowering the barrier in the double well. Finally, after a variable evolution time τ_{evol}, a second $\pi/2$ pulse (blue arrow) is applied and the final singlet fraction is measured, which oscillates at a frequency $|J_{ex}|$. **b**, Magnetic exchange in the off-resonant driving regime for $\omega/(2\pi) = 8$ kHz, $t_x/h = 350(50)$ Hz and $U/h = 2.1(1)$ kHz as a function of driving amplitude. J_{ex} decreases with K_0 as expected for a renormalized tunnelling rate t_x^{eff}. **c**, Exchange energy for near-resonant modulation with $\omega/(2\pi) = 8$ kHz, $t_x/h = 640(90)$ Hz and $U/h = 9.1(1)$ kHz (red) or $U/h = 6.5(1)$ kHz (blue) as a function of K_0. Red-detuned driving ($U > \hbar\omega$) enhances the magnetic exchange for increasing driving amplitude. For $U < \hbar\omega$, J_{ex} vanishes at a critical value $K_0 \approx 0.7$ and becomes negative for stronger driving (open symbols). The sign of the exchange is measured as shown in **d**. For $K_0 \approx 0.7$, the oscillation is too slow to determine the sign of J_{ex}. Mean values in **b** and **c** are derived from a sinusoidal fit to the data; errors denote the standard deviation obtained from a resampling method (see Methods). **d**, Sign change of the exchange energy for $U < \hbar\omega$, as indicated by the singlet fraction. The singlet fraction is shown as a function of evolution time, with $U/h = 6.5(1)$ kHz in the static case (black, grey) or after a sudden switch on of the modulation with $K_0 = 0.88(1)$ (cyan) or $K_0 = 1.31(2)$ (brown) after a quarter exchange oscillation, and with the other parameters as in **c**. Owing to the sign reversal of J_{ex}, the rotation direction on the Bloch sphere is reversed. Solid lines are damped sinusoidal fits to the data. Error bars denote the standard deviation of 3 measurements.

interaction becomes attractive[8–10,29] (Extended Data Fig. 4, Methods). We measure J_{ex} between neighbouring sites directly in the experiment using our optical lattice with tunable geometry. For that, we disconnect individual pairs of sites in the x direction from each other by raising the potential barrier in the y and z directions, so that the coupling $t_{y,z}/h < 2$ Hz becomes negligible, and measure the exchange energy in a Ramsey-type sequence (Fig. 4a)[29,30].

The results of the measurements in the off- and near-resonant driving regimes for a modulation frequency of $\omega/(2\pi) = 8$ kHz are shown in Fig. 4. In the case of high-frequency modulation with $t_x \ll U \ll \hbar\omega$, the tunnelling is renormalized according to equation (2) and the exchange energy decreases as a function of the driving amplitude as $J_{ex} \approx 4t_x^2\mathcal{J}_0^2(K_0)/U$ (Fig. 4b). By contrast, in the near-resonant regime, the system is to lowest order described by the tunnelling process in equation (3) and we observe an increasing exchange energy as a function of the modulation strength for $\delta < 0$ (Fig. 4c). At $K_0 \approx 1.6$ it reaches a level about three times higher than in the static case. If $\delta > 0$, J_{ex} vanishes at a critical modulation amplitude of $K_0 \approx 0.7$ and changes sign for stronger driving. To demonstrate that the exchange becomes negative for large K_0, we first perform a quarter oscillation in the static double well, followed by a sudden switch on of the modulation with $K_0 > 0.7$ (ref. 29). Because the exchange in the driven double well is ferromagnetic, it inverts its rotation direction on the Bloch sphere, which leads to an oscillation phase shifted by π compared to the static case (Fig. 4d).

The dependence of the exchange energy on the driving frequency and strength provides a microscopic explanation for the phenomena observed in the many-body system. In the off-resonant case, the magnetic exchange decreases with increasing modulation amplitude, which reduces the lattice anisotropy and therefore the correlations on the x bonds (Fig. 2b). If the interaction energy U comes close to, but is still lower than the driving frequency, then resonant effects start to dominate and the magnetic exchange inverts its sign, leading to ferromagnetic correlations in the many-body system as observed in Fig. 3b, c. For $U \gtrsim \hbar\omega$, the exchange energy increases with K_0, which can enhance antiferromagnetic correlations for several reasons. First, the anisotropy is increased because the ratio $J_{ex}^x/J_{ex}^{y,z}$ becomes larger, which makes it more favourable to redistribute entropy onto the weak links in the y and z directions[24,25]. Second, while the exchange is increased, the single-particle tunnelling energy is renormalized as $t_{x,single} = t_x\mathcal{J}_0(K_0)$ in the effective Hamiltonian; see equation (3). Owing to the isolated nature of the entire system, the reduction of $t_{x,single}$ leads to an entropy redistribution in the trap and lowers the absolute temperature, which enhances magnetic correlations globally. Last, when the ratio $J_{ex}/t_{x,single}$ increases, it becomes more favourable for two atoms to pair and form a singlet state in the low filled regions of the trap instead of delocalizing far apart[9]. This process plays an important part in the context of high-temperature superconductivity, and the independent control of the exchange and tunnelling energies opens up the possibility of investigating d-wave pairing in the t–J model[7]. Further theoretical studies will be necessary to determine the degree to which these three effects are responsible for the enhancement of antiferromagnetic correlations in the many-body system.

Having shown that near-resonant driving can be used to increase or reverse the sign of magnetic correlations, the low-energy scales in systems of cold atoms enable further investigations of the timescales involved and the possible existence of pre-thermalized states in future experiments[21]. Remarkably, the lifetime of correlations in the driven many-body system was found to be sufficiently long that they could be observed even in the near-resonant driving regime. To investigate this further, the entropy increase could be studied systematically as a function of the energy scales involved and the connectivity of the underlying lattice geometry. Furthermore, by additionally imprinting complex phases on the density-assisted tunnelling energies, dynamical gauge fields and anyonic statistics could be engineered[26].

Online Content Methods, along with any additional Extended Data display items and Source Data, are available in the online version of the paper; references unique to these sections appear only in the online paper.

Received 14 July; accepted 7 November 2017.

1. Kirilyuk, A., Kimel, A. V. & Rasing, T. Ultrafast optical manipulation of magnetic order. *Rev. Mod. Phys.* **82,** 2731–2784 (2010).
2. Nicoletti, D. & Cavalleri, A. Nonlinear light-matter interaction at terahertz frequencies. *Adv. Opt. Photonics* **8,** 401–464 (2016).
3. Rini, M. *et al.* Control of the electronic phase of a manganite by mode-selective vibrational excitation. *Nature* **449,** 72–74 (2007).
4. Mariager, S. O. *et al.* Structural and magnetic dynamics of a laser induced phase transition in FeRh. *Phys. Rev. Lett.* **108,** 087201 (2012).
5. Li, T. *et al.* Femtosecond switching of magnetism via strongly correlated spin–charge quantum excitations. *Nature* **496,** 69–73 (2013).
6. Mitrano, M. *et al.* Possible light-induced superconductivity in K_3C_{60} at high temperature. *Nature* **530,** 461–464 (2016).
7. Dagotto, E. Correlated electrons in high-temperature superconductors. *Rev. Mod. Phys.* **66,** 763–840 (1994).
8. Mentink, J. H., Balzer, K. & Eckstein, M. Ultrafast and reversible control of the exchange interaction in Mott insulators. *Nat. Commun.* **6,** 6708 (2015).
9. Coulthard, J., Clark, S. R., Al-Assam, S., Cavalleri, A. & Jaksch, D. Enhancement of superexchange pairing in the periodically driven Hubbard model. *Phys. Rev. B* **96,** 085104 (2017).
10. Kitamura, S. & Aoki, H. η-pairing superfluid in periodically-driven fermionic Hubbard model with strong attraction. *Phys. Rev. B* **94,** 174503 (2016).
11. Goldman, N. & Dalibard, J. Periodically driven quantum systems: effective Hamiltonians and engineered gauge fields. *Phys. Rev. X* **4,** 031027 (2014).
12. Bukov, M., D'Alessio, L. & Polkovnikov, A. Universal high-frequency behavior of periodically driven systems: from dynamical stabilization to Floquet engineering. *Adv. Phys.* **64,** 139–226 (2015).
13. Struck, J. *et al.* Quantum simulation of frustrated classical magnetism in triangular optical lattices. *Science* **333,** 996–999 (2011).
14. Jotzu, G. *et al.* Creating state-dependent lattices for ultracold fermions by magnetic gradient modulation. *Phys. Rev. Lett.* **115,** 073002 (2015).
15. Eckardt, A. Colloquium: Atomic quantum gases in periodically driven optical lattices. *Rev. Mod. Phys.* **89,** 011004 (2017).
16. Zenesini, A., Lignier, H., Ciampini, D., Morsch, O. & Arimondo, E. Coherent control of dressed matter waves. *Phys. Rev. Lett.* **102,** 100403 (2009).
17. Parker, C. V., Ha, L.-C. & Chin, C. Direct observation of effective ferromagnetic domains of cold atoms in a shaken optical lattice. *Nat. Phys.* **9,** 769–774 (2013).
18. Ma, R. *et al.* Photon-assisted tunneling in a biased strongly correlated Bose gas. *Phys. Rev. Lett.* **107,** 095301 (2011).
19. Meinert, F., Mark, M. J., Lauber, K., Daley, A. J. & Nägerl, H.-C. Floquet engineering of correlated tunneling in the Bose-Hubbard model with ultracold atoms. *Phys. Rev. Lett.* **116,** 205301 (2016).
20. Desbuquois, R. *et al.* Controlling the Floquet state population and observing micromotion in a periodically driven two-body quantum system. *Phys. Rev. A* **96,** 053602 (2017).
21. Kuwahara, T., Mori, T. & Saito, K. Floquet-Magnus theory and generic transient dynamics in periodically driven many-body quantum systems. *Ann. Phys.* **367,** 96–124 (2016).
22. Abanin, D. A., De Roeck, W., Ho, W. W. & Huveneers, F. Effective Hamiltonians, prethermalization, and slow energy absorption in periodically driven many-body systems. *Phys. Rev. B* **95,** 014112 (2017).
23. Sciolla, B. *et al.* Competition of spin and charge excitations in the one-dimensional Hubbard model. *Phys. Rev. A* **88,** 063629 (2013).
24. Imriška, J. *et al.* Thermodynamics and magnetic properties of the anisotropic 3D Hubbard model. *Phys. Rev. Lett.* **112,** 115301 (2014).
25. Greif, D., Jotzu, G., Messer, M., Desbuquois, R. & Esslinger, T. Formation and dynamics of antiferromagnetic correlations in tunable optical lattices. *Phys. Rev. Lett.* **115,** 260401 (2015).
26. Bermudez, A. & Porras, D. Interaction-dependent photon-assisted tunneling in optical lattices: a quantum simulator of strongly-correlated electrons and dynamical gauge fields. *New J. Phys.* **17,** 103021 (2015).
27. Itin, A. & Katsnelson, M. Effective Hamiltonians for rapidly driven many-body lattice systems: induced exchange interactions and density-dependent hoppings. *Phys. Rev. Lett.* **115,** 075301 (2015).
28. Bukov, M., Kolodrubetz, M. & Polkovnikov, A. Schrieffer-Wolff transformation for periodically driven systems: strongly correlated systems with artificial gauge fields. *Phys. Rev. Lett.* **116,** 125301 (2016).
29. Trotzky, S. *et al.* Time-resolved observation and control of superexchange interactions with ultracold atoms in optical lattices. *Science* **319,** 295–299 (2008).
30. Chen, Y.-A. *et al.* Controlling correlated tunneling and superexchange interactions with ac-driven optical lattices. *Phys. Rev. Lett.* **107,** 210405 (2011).

Acknowledgements We thank D. Abanin, D. Greif, D. Jaksch, M. Landini, Y. Murakami, N. Tsuji, P. Werner and W. Zwerger for discussions. We acknowledge SNF (Project Number 200020_169320 and NCCR-QSIT), Swiss State Secretary for Education, Research and Innovation Contract No. 15.0019 (QUIC) and ERC advanced grant TransQ (Project Number 742579) for funding.

Author Contributions All authors contributed extensively to the work presented in this manuscript.

Author Information Reprints and permissions information is available at www.nature.com/reprints. The authors declare no competing financial interests. Readers are welcome to comment on the online version of the paper. Publisher's note: Springer Nature remains neutral with regard to jurisdictional claims in published maps and institutional affiliations. Correspondence and requests for materials should be addressed to T.E. (esslinger@phys.ethz.ch).

Reviewer Information *Nature* thanks J. Freericks and D. Huse for their contribution to the peer review of this work.

METHODS

Optical lattice. The tunable three-dimensional optical lattice is created by a combination of four orthogonal, retroreflected laser beams of wavelength $\lambda = 1{,}064$ nm, as shown in Fig. 1a. Whereas the $\bar{X}$ and $\tilde{Y}$ beams are interfering and actively phase-locked to $\varphi = 0.00(3)\pi$, the X and Z beams are non-interfering, owing to a frequency detuning. Our optical set-up is described by the following potential[31]:

$$\begin{aligned} V(x,y,z) = &- V_{\bar{X}}\cos^2(kx+\theta/2) - V_X\cos^2(kx) \\ &- V_{\tilde{Y}}\cos^2(ky) - V_Z\cos^2(kz) \\ &- 2\alpha\sqrt{V_X V_Z}\,\cos(kx)\cos(kz)\cos(\varphi) \end{aligned} \quad (4)$$

with $k = 2\pi/\lambda$ and $V_{\bar{X},X,\tilde{Y},Z}$ the lattice depths in units of the recoil energy $E_R = h^2/(2m\lambda^2)$ of each laser beam in the three directions x, y and z (h is the Planck constant and m the mass of the atoms). The lattice potential is adjusted to fix $\theta = 1.000(2)\pi$. We calibrate the visibility of the interference term $\alpha = 0.92(1)$ with amplitude modulation of the lattice depth for different configurations of the optical potential using a ^{87}Rb Bose–Einstein condensate. To calibrate the individual lattice depths $V_{\bar{X},X,\tilde{Y},Z}$ we perform Raman–Nath diffraction on the Bose–Einstein condensate. For the calculation of tight-binding parameters, we include a systematic error of 3% for all lattice depths.

Preparation of the degenerate Fermi gas in the optical lattice. The starting point of our experiment is a balanced mixture of the $F = 9/2$, $m_F = -9/2$ and $F = 9/2$, $m_F = -7/2$ hyperfine states of ^{40}K, confined in an optical harmonic trap. We evaporatively cool the mixture to a quantum degenerate cloud with a repulsive s-wave scattering length of $115.6(8)a_0$ (a_0 denotes the Bohr radius). After the evaporation, we end up with about $3.0(2) \times 10^4$ (10% systematic error) atoms at a temperature of $T/T_F = 0.07(1)$ (T_F denotes the Fermi temperature, see Extended Data Table 1 for details). Afterwards, we either keep a mixture of the $F = 9/2$, $m_F = -9/2$ and $F = 9/2$, $m_F = -7/2$ hyperfine states to access attractive or weak repulsive interactions with scattering lengths $-3{,}000a_0 < a < 150a_0$ (measurements in Figs 2 and 4b and for the initial preparation of isolated double wells in Fig. 4), or transfer the $F = 9/2$, $m_F = -7/2$ state to the $F = 9/2$, $m_F = -5/2$ state with a radio-frequency sweep to access large repulsive scattering lengths above $200a_0$ (measurements in Figs 3 and 4c, d). For this mixture, we obtain temperatures of $T/T_F = 0.12(2)$ in the harmonic trap. The interactions can be tuned via two magnetic Feshbach resonances located at a field of 202.1 G (for $m_F = -9/2$ and $m_F = -7/2$) or 224.2 G (for $m_F = -9/2$ and $m_F = -5/2$). From this point, two distinct schemes are used to prepare atoms either in a three-dimensional hexagonal lattice (Figs 2, 3) or in isolated double wells (Fig. 4). To load a many-body state into the hexagonal lattice, we first ramp up the power of all lattice beams in 50 ms to an intermediate value. In this configuration, the tunnelling energies are close to the final configuration with $(t_x, t_y, t_z)/h = (550(30), 143(8), 156(9))$ Hz, but the horizontal link across the hexagonal unit cell still has a finite value of 70(3) Hz. In addition, the mean trap frequency is only $\bar{\omega}_{trap} = 68(2)$ Hz. In the second step, we ramp up the power in all beams in 20 ms to the final configuration (Extended Data Table 1). To load isolated double wells, we first tune the interactions to a large attractive value of $-3{,}000(600)a_0$; see ref. 20 for more details. In short, the atoms are first loaded into the lowest band of a checkerboard configuration with $V_{\bar{X},X,\tilde{Y},Z} = [0, 3, 7, 3]E_R$ using an S-shaped lattice ramp of 200 ms. Owing to the large attractive interactions during the loading process, 68(3)% of the atoms form double occupancies. In the second step, we tune the scattering length to $115.6(8)a_0$ and split each lattice site by linearly increasing $V_{\bar{X}}$ and decreasing V_X to a $V_{\bar{X},X,\tilde{Y},Z} = [30, 0, 30, 30]E_R$ cubic configuration within 10 ms. During the splitting process, the double occupancies in the checkerboard lattice are transformed into singlet states $|s\rangle = (|\uparrow,\downarrow\rangle - |\downarrow,\uparrow\rangle)/\sqrt{2}$ in the cubic lattice.

Detection methods. The detection scheme of double occupancies and nearest-neighbour spin–spin correlations follows closely the procedure used in previous work[25,32]. To characterize the atomic state, we first freeze the evolution by quenching the lattice to $V_{\bar{X},X,\tilde{Y},Z} = [30, 0, 30, 30]E_R$ within 100 μs. To detect double occupancies, we ramp the magnetic field close to the magnetic Feshbach resonance of the $m_F = -9/2$ and $m_F = -7/2$ mixture. We then selectively transfer one of the atoms sitting on doubly occupied sites from the $m_F = -7/2$ state to the $m_F = -5/2$ state, or vice versa, via a radio-frequency sweep by using the interaction shift. The number of atoms in the different Zeeman sublevels can then be determined by applying a Stern–Gerlach pulse during the time-of-flight imaging. For the measurement of spin–spin correlations, we apply a magnetic-field gradient after the lattice freeze. This leads to coherent oscillations between the magnetic singlet state $|s\rangle = (|\uparrow,\downarrow\rangle - |\downarrow,\uparrow\rangle)/\sqrt{2}$ and triplet state $|t\rangle = (|\uparrow,\downarrow\rangle + |\downarrow,\uparrow\rangle)/\sqrt{2}$ on neighbouring sites in the x direction. The singlet fraction p_s can be determined by merging adjacent lattice sites by going to a $V_{\bar{X},X,\tilde{Y},Z} = [0, 30, 30, 30]E_R$ checkerboard configuration within 10 ms. This procedure transforms the singlet into a double occupancy in the single well, which can again be measured as outlined above. The triplet fraction p_t is obtained by applying a π pulse with the magnetic-field gradient and subsequently measuring the singlet fraction. The spin–spin correlation is then obtained as $\mathcal{C} = -\langle \hat{S}_i^x \hat{S}_{i+1}^x \rangle - \langle \hat{S}_i^y \hat{S}_{i+1}^y \rangle = (p_s - p_t)/2$. We average all observables over one period $T = 2\pi/\omega$ of the drive to be insensitive to the micromotion. For that, we vary slightly the total duration of the modulation between different measurements by multiples of $T/4$ to sample different phases of the modulation cycle. For the measurement of double occupancies in the hexagonal lattice (Figs 2a, 3a) we sample four different times during the modulation cycle, whereas for the magnetic correlations (Figs 2b, 3b, c, Extended Data Figs 1, 2) we measure for five different times and take each data point two or three times (see captions for the exact number of measurements). For the measurements performed in the isolated double wells (Fig. 4) the observables were not averaged over one driving period because we have experimentally verified that no fast dynamics could be observed in this configuration. This can be explained by $\hbar\omega$ being much larger than t.

Periodic driving. The periodic driving is implemented as in previous work[20]. In brief, a piezo-electric actuator enables a controlled phase shift of the reflected X and $\bar{X}$ lattice beams with respect to the incoming beams. To access the driven regime, we modulate the lattice position by a sinusoidal movement of the mirror position for the retroreflecting lattice beam at frequency $\omega/(2\pi)$. We choose the modulation to be along the direction of the horizontal bonds such that $V(x, y, z, \tau) \equiv V(x - A\cos(\omega\tau), y, z)$. We linearly ramp up a sinusoidal modulation and then maintain a fixed displacement amplitude A. During the modulation we ensure the correct phase relation $\varphi = 0.0(1)\pi$ between the two interfering X and Z lattice beams by modulating the phase of the respective incoming beams at the same frequency using acousto-optical modulators. In addition, this phase modulation is used to calibrate the phase and amplitude of the mirror displacement. In our set-up, the piezo modulation also leads to a residual periodic reduction in the interference amplitude of the lattice by at most 2%. For the lattice configurations used in our experiments, this shifts the mean tunnelling energy t_x down by about 2.5% and introduces a modulation of the tunnelling energy at twice the driving frequency $2\omega/(2\pi)$ with an amplitude of $\delta t = 0.025t_x$. The effect of the modulation is negligible because its amplitude has to be compared to the driving frequency. The effective driving strength is $\delta t/(\hbar\omega)$, which is always less than 3×10^{-3} in our case. In addition, we have verified that our experimental findings are not affected by the launching phase of the drive. The amplitude of the lattice displacement A is related to the normalized driving amplitude directly: $K_0 = mA\omega d_x/\hbar$, where d_x is the distance between the two sites along the x direction. For our lattice potential, $d_x \neq \lambda/2$ and must be calculated for each individual configuration. To this end, we determine the Wannier functions located on the left and right sides of the bond considered, which are derived as the eigenstates of the band-projected position operator. The distance d_x is then evaluated as the difference between the eigenvalues of two neighbouring Wannier states, and is given in Extended Data Table 1 for all lattice configurations. In addition, because the lattice geometry in the x–z plane is not an ideal brick configuration, the bonds connecting two sites in the z direction are also slightly affected by the drive. The effective driving strength can be determined by the projected bond length on the modulation direction, which for our case is the x displacement $d_x^{vert} = \lambda/2 - d_x$ between neighbouring sites in the vertical z direction. The modulation amplitude is then $K_0^{vert} = d_x^{vert}/(d_x K_0)$. The values for d_x^{vert} are given in Extended Data Table 1 for our lattice configurations.

Calibration of the on-site interactions. The extension of the Wannier function can be similar to the scattering length for strong interactions in the optical potentials realized in our measurements. Thus, the actual on-site interaction strength U may be altered compared to the value calculated by using the non-interacting Wannier functions, as observed in previous experiments[20,33]. We therefore determine U experimentally by driving the lattice at a frequency $\omega/(2\pi)$ and measure the number of double occupancies as a function of U. Double occupancies are maximally created either for $\hbar\omega = U$ in a connected lattice (Figs 2, 3) or for $\hbar\omega = (\sqrt{U^2 + 16t^2} + U)/2$ in the isolated double wells (Fig. 4). In the hexagonal lattice, the resonance position agrees within the uncertainty of the numerical value for U determined from the Wannier function, as shown in Fig. 3a. However, a substantial difference is observed in the isolated double wells. To account for this effect, we parameterize U by $U(a) = \alpha a(1 - a/a_c)$, where α is given by the non-interacting Wannier functions and a_c is a higher-order correction that depends on the lattice depth. For the isolated double wells, we find $a_c = 4{,}800(300)a_0$, which leads to a reduction in U of about 10% with respect to the calculated value for the datasets shown in Fig. 4c. Accordingly, this correction is incorporated into all interaction strengths given for the isolated double wells.

Validity of tight-binding approximation and higher band effects. When deriving the tight-binding Hamiltonian of the driven Fermi–Hubbard model in equation (1),

we assume that the Wannier functions are not modified by the modulation. However, for large driving amplitudes a substantial tilt is applied to the lattice in the co-moving frame, which introduces an energy bias $\hbar\omega K_0$ between neighbouring sites (see also Fig. 1). As a result, the Wannier functions will be modified by the admixture of higher-band Wannier functions of the untilted lattice. This will in turn lead to different tight-binding parameters t_x and U at any given time within the modulation cycle. To estimate the corrections that result from the change in the Wannier functions, we consider a cut through the tilted lattice potential in the x direction of the modulation. This potential can be very well approximated around the horizontal bonds by a lattice with a relative phase $\theta \neq \pi$ between the lattice beams $\bar{X}$ and X (see equation (4)). The approximation in this step is to assume that all lattice sites in a given sublattice ($\mathcal{A}$ or $\mathcal{B}$) are at equal energy. This is well justified for our lattice geometry because the tunnelling energy across the hexagon is zero and so the Wannier functions on the $\mathcal{A}$ sublattice, for example, are not influenced by the $\mathcal{B}$ sites to their left. Because the discrete spatial periodicity is restored in the lattice potential with $\theta \neq \pi$, we can compute the Wannier functions for any given energy bias and calculate the corresponding tight-binding parameters. The modulated lattice potential can then be described by a tight-binding Hamiltonian as in equation (1), where in addition to the oscillating force $f(\tau)$ the Hubbard parameters $t_x(\tau)$ and $U_{\mathcal{A},\mathcal{B}}(\tau)$ become time- and sublattice-dependent. We decompose the parameters into their Fourier components, which take the form

$$\begin{aligned} t_x(\tau) &= t_x(K_0=0) + \delta t_0(K_0,\omega) + \delta t_2(K_0,\omega)\cos(2\omega\tau) + \cdots \\ U_{\mathcal{A}}(\tau) &= U(K_0=0) + \delta U_0(K_0,\omega) + \delta U_1(K_0,\omega)\cos(\omega\tau) \\ &\quad + \delta U_2(K_0,\omega)\cos(2\omega\tau) + \cdots \\ U_{\mathcal{B}}(\tau) &= U_{\mathcal{A}}(\tau+\pi/\omega) \end{aligned}$$

The expansion of $t_x(\tau)$ features only even harmonics of ω because $t_x(\tau)=t_x(\tau+\pi/\omega)$. The main effect of the modulation is a shift in the static tunnelling energy by $\delta t_0(K_0, \omega)$, which is given in Extended Data Table 1 for the maximum driving amplitude and frequency in each lattice configuration. Note that even though the relative change in the tunnelling energy is around 10%–20% for large values of K_0, the absolute change is much smaller because the hopping amplitude is renormalized by the Bessel function $\mathcal{J}_0(K_0)$ or $\mathcal{J}_1(K_0)$, depending on the frequency regime. On the other hand, we find that the shift in the mean value of U is much smaller, and even for the strongest driving we have $\delta U_0(K_0, \omega)/U < 6\times10^{-3}$. The second effect is a modulation of t_x and U, which is negligible because it has to be compared to the driving frequency. The dimensionless modulation strength for the lowest Fourier components will be given by $K_0^t = \delta t_2(K_0,\omega)/(2\hbar\omega)$ and $K_0^U = \delta U_1(K_0,\omega)/(\hbar\omega)$. Even for the maximum values of K_0 and ω, we find $K_0^t < 6\times10^{-3}$ and $K_0^U < 0.02$ for all of our lattice geometries. We also performed a numerical simulation of the two-site Hubbard model including all of the above modifications, in which we use a Trotter decomposition to evaluate the quasi-energy spectrum (see also Methods section 'Theoretical treatment of the driven double well' and Extended Data Fig. 4). We have found that even for the largest driving amplitudes used in the measurement of the exchange energy (see Fig. 4), J_{ex} is modified by at most 10 Hz in the off-resonant driving regime (compare to Extended Data Fig. 4b) and 60 Hz in the near-resonant case (Extended Data Fig. 4d), which is caused mainly by the shift in the mean value of t_x. This change is still smaller than or comparable to the uncertainty on the exchange energy that results from an imprecise calibration of the Hubbard parameters in the lattice, which is around 70 Hz.

Measurement of magnetic exchange. The exchange energy is measured in a Ramsey-type protocol in isolated double wells. After preparing singlet states on adjacent sites in a deep cubic lattice with $V_{\bar{x},X,\bar{Y},Z} = [30, 0, 30, 30]E_R$ as outlined above, we perform a $\pi/2$ pulse with a magnetic-field gradient to generate a coherent superposition between the singlet and triplet states. After this, we first ramp the magnetic field, the interfering lattice V_X and the driving amplitude K_0 to the desired value within 2 ms. In the next step, we trigger an exchange oscillation by suddenly lowering the barrier in the double well by decreasing $V_{\bar{X}}$ to the desired value within 100 μs. After a variable evolution time τ_{evol} in the driven system, we freeze the dynamics again by increasing $V_{\bar{X}}$ to $30E_R$ within 100 μs, revert the ramps of the magnetic field, the interfering lattice V_X and the driving amplitude K_0, and perform a second $\pi/2$ pulse with a magnetic-field gradient. Finally, we measure the fraction of singlet states on adjacent sites, which after the evolution is $p_s(\tau_{evol}) = [1 - \cos(J_{ex}\tau_{evol}/\hbar)]/2$. In the experiment, we vary the evolution time τ_{evol} and measure the singlet fraction for each modulation amplitude K_0 for not fewer than 9 different values of τ_{evol}, with at least 27 individual measurements in total. We fit the data with a function $p_s(\tau_{evol}) = \alpha[1 - \cos(J_{ex}\tau_{evol}/\hbar)]\exp(-\beta\tau) + \gamma$ and extract the exchange from the fitted frequency. To estimate the error, we use a resampling method that assumes a normal distribution of measurement results at each evolution time. The standard deviation of the distribution is determined by the measured standard deviation or, if we measured the singlet fraction at this τ_{evol} only once, by the residual from the fitted curve. Afterwards, we randomly sample a value for the singlet fraction at each evolution time and refit the resulting dataset. At the same time, the initialization values of the fit parameters J_{ex} and β are varied by ±10%. This procedure is repeated 1,000 times and the mean ± standard deviation of the resulting distribution of frequencies determines the asymmetric error bars for the fitted exchange frequency, as shown in Fig. 4. To demonstrate the sign change of the magnetic exchange for $U \lesssim \hbar\omega$ (Fig. 4d), we first let the system evolve for a time τ_0 with a non-driven exchange $J_{ex}^{(0)}$ until a quarter exchange oscillation has been performed, that is, $J_{ex}^{(0)}\tau_0 = \pi/2$. After that, we suddenly switch on the sinusoidal modulation at the desired value of K_0, which projects the system onto a Hamiltonian with a negative J_{ex}. Therefore, the system changes its sense of rotation on the Bloch sphere (Fig. 4a) and the singlet fraction after a variable total evolution time $\tau_{evol} > \tau_0$ is given by $p_s(\tau_{evol}) = \{1 + \mathrm{sgn}(J_{ex}) \times \sin[|J_{ex}|(\tau_{evol} - \tau_0)/\hbar]\}/2$.

Theoretical treatment of the driven double well. We perform both analytic and numerical studies on the driven double well, as described in earlier work[20]. In this context, we use Floquet's theorem to derive an effective static Hamiltonian in a high-frequency expansion. In the following, we include terms up to order $1/\omega$, as given in appendix A in ref. 20. In the off-resonant case, the term proportional to $1/\omega$ vanishes, such that the effect of the modulation is a pure renormalization of the tunnelling by a zeroth-order Bessel function $t \to t\mathcal{J}_0(K_0)$. Therefore, the exchange energy defined as the energy difference between the triplet and singlet state becomes

$$J_{ex,off\text{-}res} = \frac{1}{2}\left[-U + \sqrt{16t^2\mathcal{J}_0^2(K_0) + U^2}\right]$$

In the Heisenberg limit of large interactions ($t \ll U \ll \hbar\omega$) we find

$$J_{ex,off\text{-}res} \xrightarrow{U\gg t} 4\frac{t^2}{U}\mathcal{J}_0^2(K_0) \tag{5}$$

In the case of near-resonant driving ($t \ll U \approx \hbar\omega$), we can express the Hamiltonian in terms of t, U and the detuning $\delta = \hbar\omega - U$, and we consider terms up to orders $\mathcal{O}(t^2/U, t\delta/U, \delta^2/U)$. In this regime, the single-particle tunnelling $t_0 = t\mathcal{J}_0(K_0)$ is renormalized as for the off-resonant case. On the other hand, the density-assisted tunnelling that changes the number of double occupancies is given by $t_1 = t\mathcal{J}_1(K_0)$. The exchange for $\delta \gtrless 0$ is given by

$$J_{ex,res} = \frac{1}{2}\left[\delta + 4\frac{t_0^2}{U} \mp \sqrt{16t_1^2 + \left(\delta - 4\frac{t_0^2 + t_1^2}{U}\right)^2}\right]$$

which reproduces the Heisenberg limit in equation (5) for the case of no driving ($K_0 = 0$). For large detunings ($t \ll \delta \ll U, \hbar\omega$), the exchange takes the form

$$J_{ex,res} \xrightarrow{\delta\gg t} -4\frac{t_1^2}{\delta} + 2\frac{2t_0^2 + t_1^2}{U}$$

The leading term of this expansion is proportional to $\mathcal{J}_1^2(K_0)$ and changes sign with the detuning δ. This explains the switch to a ferromagnetic exchange for $U < \hbar\omega$ beyond a certain driving strength. In addition to the analytic derivation of the effective Hamiltonian, we also perform a numerical simulation of the two-site Hubbard model. We use a Trotter decomposition to evaluate the evolution operator over one period, from which we extract the spectrum (for details see ref. 20). A comparison of the numerical and analytic results for the experimental parameters is shown in Extended Data Fig. 4. For all of the derivations above, we assume that the static double well can simply be described by the tunnelling t and the on-site interaction U. However, if the Wannier functions on the two sites have a substantial overlap, then the description needs to be extended to a two-band Hubbard model. In this case, higher-order corrections such as density-assisted tunnelling δt, as well as nearest-neighbour interactions, direct exchange and correlated pair tunnelling V (the last three are all equal for the two-band Fermi–Hubbard model), become important (see appendix A.1 in ref. 20). For the experimental parameters in the off-resonant case (Fig. 4b), the values of these higher-order corrections are $V/h = 2.4(7)$ Hz and $\delta t/h = 22(3)$ Hz in the static lattice. In the near-resonant driving regime (Fig. 4c), interactions are stronger and the corrections increase to $V/h = 26(8)$ Hz and $\delta t/h = 120(10)$ Hz for $U/h = 6.5(1)$ kHz, and

$V/h = 40(10)$ Hz and $\delta t/h = 170(20)$ Hz for $U/h = 9.1(1)$ kHz. To lowest order, the density-assisted tunnelling will increase the effective tunnelling to $t + \delta t$, and V decreases the exchange interaction by $2V$, in both the static and driven cases.

Data availability. All data files are available from the corresponding author on request. Source Data for Figs 2–4 and Extended Data Figs 1–3 are provided with the online version of the paper.

31. Tarruell, L., Greif, D., Uehlinger, T., Jotzu, G. & Esslinger, T. Creating, moving and merging Dirac points with a Fermi gas in a tunable honeycomb lattice. *Nature* **483,** 302–305 (2012).
32. Greif, D., Uehlinger, T., Jotzu, G., Tarruell, L. & Esslinger, T. Short-range quantum magnetism of ultracold fermions in an optical lattice. *Science* **340,** 1307–1310 (2013).
33. Uehlinger, T. *et al.* Artificial graphene with tunable interactions. *Phys. Rev. Lett.* **111,** 185307 (2013).

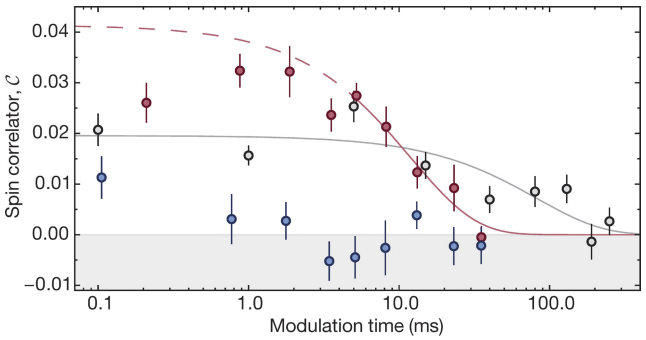

Extended Data Figure 1 | Time dependence of magnetic correlations for near-resonant driving. Nearest-neighbour spin–spin correlator $\mathcal{C}$ for the same lattice configuration as in Fig. 3, as a function of the modulation time after the ramp up of the drive. The data allow us to compare the formation and decay of magnetic correlations for two specific sets of interactions and modulation frequencies with the level of correlations in the static case (black). For a driving strength of $K_0 = 1.30(3)$ and with $U/h = 3.8(1)$ kHz and $\omega/(2\pi) = 3$ kHz (red), antiferromagnetic correlations increase with time and reach a level higher than the static case (black, $U/h = 3.8(1)$ kHz). If the interaction is smaller than the driving frequency (blue, $U/h = 4.4(1)$ kHz, $\omega/(2\pi) = 6$ kHz), then the correlations switch sign and become ferromagnetic after a few milliseconds. For long times, the correlations in each configuration decrease as a result of heating in the lattice. Solid lines show exponential fits of the full data in the static case (grey) and to modulation times longer than 4 ms in the driven lattice for $U > \hbar\omega$ (red). The difference between the data and the dashed component of the fit (red) indicates an initial increase in the correlations. The extracted lifetimes decrease from 82(34) ms without drive to 12(4) ms at $K_0 = 1.30(3)$. All measurements are averaged over one modulation cycle. Data points and error bars denote the mean and standard error of 13 individual measurements at different times within one driving period (see Methods).

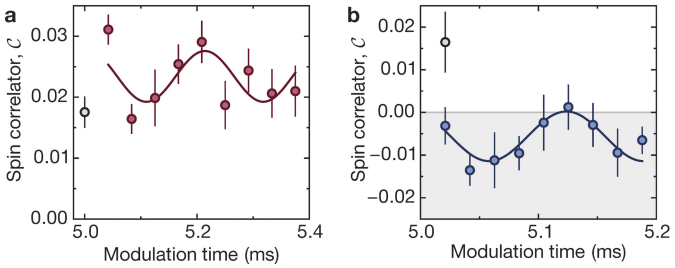

Extended Data Figure 2 | Micromotion for near-resonant driving. **a**, **b**, Nearest-neighbour spin–spin correlator $\mathcal{C}$ for the lattice configuration in Fig. 3 and $K_0 = 1.30(3)$, as a function of modulation time after the ramp up of the drive, sampled within one oscillation period. We observe substantial micromotion both for the case of enhanced antiferromagnetic correlations (**a**; $U/h = 3.8(1)$ kHz and $\omega/(2\pi) = 3$ kHz) and for ferromagnetic correlations (**b**; $U/h = 4.4(1)$ kHz and $\omega/(2\pi) = 6$ kHz). For a different set of parameters in the measurement of the micromotion it should be also possible to switch between antiferromagnetic and ferromagnetic correlations within one driving cycle. The open symbols represent a reference measurement in the static case with all other parameters being equal. Solid lines are sinusoidal fits to the data, which results in a fitted frequency of $4.8^{+1.9}_{-0.4}$ kHz (**a**) or $7.6^{+3.9}_{-1.7}$ kHz (**b**). Error bars denote the standard error of 10 independent measurements.

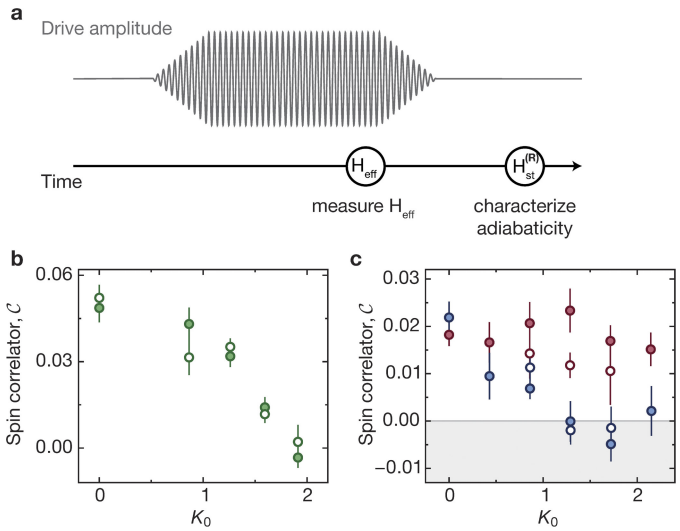

Extended Data Figure 3 | Adiabaticity of the modulation ramp in the many-body system. a, Starting from the static lattice, the modulation amplitude is ramped up and subsequently kept at a fixed value to allow for a 5 ms equilibration time. The ramp up time depends on the chosen configuration and is 3.333 ms (2 ms) for a modulation frequency of $\omega/(2\pi) = 3$ kHz (6 kHz). We start the detection of nearest-neighbour spin–spin correlations $\mathcal{C}$ in the effective Hamiltonian H_{eff} by quenching the tunnelling to zero as we ramp up the lattice depth in all directions during the modulation within 100 μs. To estimate the adiabaticity of the final state, we perform a second type of measurement in which we revert the driving ramp and subsequently wait an additional 5 ms before the detection in the reverted static Hamiltonian $H_{\mathrm{st}}^{(R)}$. If the ramp scheme of the modulation is fully adiabatic, we expect a reversal of the correlations to their static value. **b**, The nearest-neighbour spin–spin correlator $\mathcal{C}$ is plotted against the modulation amplitude in the off-resonant driving regime ($U/h = 0.93(2)$ kHz, $\omega/(2\pi) = 6$ kHz). The filled green circles are measured in the modulated system (same data as in Fig. 2b) and the open green circles after ramping off the modulation. The correlations no longer reach the level of the static case at $K_0 = 0$ after reverting the ramp. We attribute this to some extent to a reduced lifetime of correlations, which is found to be 14(5) ms at $K_0 = 1.26(4)$, compared to 92(16) ms in the static case. **c**, Spin–spin correlator for different driving strengths K_0 in the near-resonant regime for $U < \hbar\omega$ (blue; $U = 4.4(1)$ kHz, $\omega/(2\pi) = 6$ kHz) and in the regime of enhanced antiferromagnetic correlations (red; $U/h = 3.8(1)$ kHz, $\omega/(2\pi) = 3$ kHz). Filled data points represent the effective states in the modulated system and open data points are measured after ramping off the modulation. Again, correlations do not reach the static value after reverting the driving ramp, owing to the finite lifetime (see also Extended Data Fig. 1). Data points and error bars denote the mean and standard error of 10 individual measurements at different times within one driving period (see Methods).

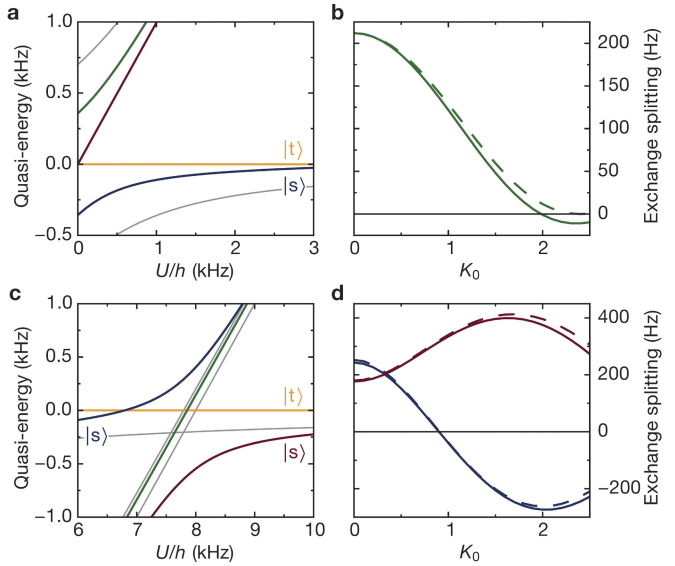

Extended Data Figure 4 | Analytical and numerical treatment of a driven double well. a, Quasi-energy spectrum for two particles in a double well as a function of the onsite interaction U for off-resonant driving ($t/h = 350$ Hz, $K_0 = 1.5$, $\omega/(2\pi) = 8$ kHz). Each of the four Floquet states representing the quasi-energy spectrum is shown in a distinct colour. The grey lines show the energy spectrum without modulation. For $U \gg t$, the ground state is the spin singlet $|\mathrm{s}\rangle$ and the first excited state is the triplet $|\mathrm{t}\rangle$. To lowest order, the driving renormalizes the tunnelling by a zeroth-order Bessel function $t_x \rightarrow t_x^{\mathrm{eff}}(K_0) = t_x \mathcal{J}_0(K_0) \approx 0.51 t_x$. **b**, Calculated exchange energy $J_{\mathrm{ex,off\text{-}res}}$ (see Methods), defined as the energy difference between the spin singlet and triplet states (see **a**), as a function of the driving amplitude K_0 for an off-resonant modulation ($t/h = 350$ Hz, $U/h = 2.1$ kHz, $\omega/(2\pi) = 8$ kHz; compare with Fig. 4b). The dashed line is the analytical result derived from a high-frequency expansion of the effective Hamiltonian; the solid line is the result of a numerical calculation. The exchange energy is reduced to small values as the tunnelling is renormalized by the zeroth-order Bessel function $\mathcal{J}_0(K_0)$. For large modulation amplitudes, deviations from the result obtained from an expansion up to order $1/\omega$ can be observed. Here, the exchange already becomes weakly ferromagnetic owing to the finite value of the interaction. **c**, Floquet spectrum of the double-well system as a function of the interactions U for near-resonant driving ($t/h = 640$ Hz, $K_0 = 0.8$, $\omega/(2\pi) = 8$ kHz). The grey lines show the energy spectrum without periodic modulation. The drive couples the singlet state to a state that contains double occupancy, which leads to an avoided crossing at $U \approx \hbar\omega$. As a result, a gap opens that is to lowest order given by $4\mathcal{J}_1(K_0)$. **d**, Dependence of the exchange energy $J_{\mathrm{ex,res}}$ on the modulation amplitude in the near-resonant regime for two different detunings with $t/h = 640$ Hz and $\omega/(2\pi) = 8$ kHz (blue, $U/h = 6.5$ kHz; red, $U/h = 9.1$ kHz; compare with Fig. 4c). The dashed line is the analytical result (see Methods) derived from a high-frequency expansion of the effective Hamiltonian; the solid line is the result of a numerical calculation. For $U > \hbar\omega$ the exchange energy is greatly increased, whereas for $U < \hbar\omega$ it changes sign to ferromagnetic behaviour. In both driving regimes, the analytical result is in very good agreement with the numerics. Our measurements of the exchange energy in Fig. 4 agree well on a qualitative level with the theoretical expectation.

Extended Data Table 1 | Summary of experimental parameters

Main text figure	2	3	4b	4c, 4d
Atom number (10^3)	28(2)	32(2)	186(6)	
Initial T/T_F	0.07(1)	0.12(2)	0.06(1)	
$\bar{\omega}_{trap}/2\pi$ (Hz)	84(2)	84(2)	119(2)	
t_x/h (Hz)	810(150)	570(110)	350(50)	640(90)
t_y/h (Hz)	125(8)	125(8)	< 1	
t_z/h (Hz)	78(8)	85(8)	< 2	
$d_x/(\lambda/2)$	0.71(2)	0.74(2)	0.79(1)	0.73(1)
$d_x^{vert}/(\lambda/2)$	0.29(2)	0.26(2)	0.21(1)	0.27(1)
$\delta t_0(K_0^{max}, \omega^{max})/t_x$	0.085(1)	0.102(1)	0.236(9)	0.106(2)

Values given for Fig. 2 correspond to the initial static configuration with $K_0 = 0$. The initial temperature is measured before loading the atoms into the lattice. d_x is the length of the horizontal bonds; d_x^{vert} is the horizontal distance between two sites that form the vertical bonds in the z direction, which results from a non-rectangular unit cell. The effective modulation amplitude is given by the projection of each bond on the x direction. δt_0 describes the change in the mean value of t_x in the driven lattice due to a time-dependent modification of the Wannier functions. The values given here are upper bounds corresponding to the maximum modulation amplitude K_0^{max} and frequency ω^{max} used in each lattice configuration (see Methods for further details).